Simulations and experiments of phase separation in binary dusty plasmas

Stefan Schütt* and André Melzer
Institute of Physics, University of Greifswald, 17489 Greifswald, Germany

(Received 19 February 2021; accepted 16 April 2021; published 5 May 2021)

Molecular dynamics simulations of binary dusty plasmas have been performed and their behavior with respect to the phase separation process has been analyzed. The simulated system was inspired by experimental research on phase separation in dusty plasmas under microgravity on parabolic flights. Despite vortex formation in the experiment and in the simulations the phase separation could be identified. From the simulations it is found that even the smallest charge disparities lead to phase separation. The separation is due to the force imbalance on the two species and the separation becomes weaker with increasing mean particle size. In comparison, experiments on the phase separation have been performed and analyzed in view of the separation dynamics. It is found that the experimental results are reproduced by the simulation regarding the dependency on the size disparity of the two particle species.

DOI: 10.1103/PhysRevE.103.053203

I. INTRODUCTION

Phase separation processes can be observed in many different fields. They have been studied in very different systems such as critical binary liquids, polymers, colloidal systems, and metallic alloys [1–8]. In many cases, binary systems are used to study fundamental phase separation processes. Such binary systems, i.e., systems in which only two different species are present, are the simplest possible system that can exhibit phase separation and thus allows insights into the basic processes.

Here we will analyze phase separation in binary dusty plasmas. In addition to neutral gas and a plasma of electrons and ions, binary dusty plasmas consist of two different types of dust particles. Such binary dusty plasmas are known to show phase separation [9–19]. Since in typical laboratory discharges most of the acting forces depend on the particle radius, binary dusty plasmas can be characterized by their (relative) size disparity $\varepsilon = (a_2 - a_1)/\bar{a}$, where a_1 and a_2 are the radii of the two species and $\bar{a}$ is their mean.

Early experiments [9–14] and simulations [15–17] on binary dusty plasmas used relatively large size disparities. For size disparities above a certain threshold, it is expected that the two populations separate due to spinodal decomposition [20,21] that relies on the nonadditivity of the particle-particle interaction. In the experiments it was found, however, that phase separation can be observed in dusty plasmas even at much smaller size disparities which was attributed to a difference of the plasma forces due to the different particle radii [18]. Recently, we have performed a systematic study of phase separation in three-dimensional binary dusty plasmas under microgravity conditions using parabolic flights [19]. There it was found that the phase separation of two species is more pronounced with larger size disparity and that phase separation occurs even at the smallest investigated ε. Other influences like the absolute particle size $\bar{a}$ and plasma conditions played only a minor role. In the experiments, due to the acting forces, the larger particles accumulate at the outer parts of the three-dimensional dust cloud, whereas the smaller particles accumulate in the center.

One problem of the experiments is that the phase separation starts immediately on dust injection and that a good part of the separation process has already occurred before the dust cloud reaches a steady state. It is therefore not possible to track the whole separation process from the beginning on. Here we present molecular dynamics (MD) simulations of different binary dust systems that allow us to study the entire separation process. We use the LAMMPS code to model the MD behavior of the dust particles. Here, we specifically aim to model a situation that is close to the experimental situation. For further analysis, we also use adapted geometries to study the influence of the curl and the divergence of the (realistic) force field. The relevant interaction forces have been derived from a SIGLO simulation of the plasma components. Results will be compared with our experimental findings. Furthermore, the simulations allow to vary parameters more easily and in a more controlled way, whereas the number of parameter variations in the experiment is limited by the number of parabolas that can be flown during a measurement campaign. Especially the amount of dust particles injected into the plasma by electromagnetic dust shakers can only be controlled in a very limited way, so that simulations with a well-known particle number are a welcome complement to the measurements.

The simulations will be checked against the experimental results. Therefore, data from Ref. [19] have been reanalyzed using a refined technique and new data have been obtained from the 2019 and 2020 parabolic flight campaigns.

In the following section, we will briefly recapitulate the experimental setup of the measurements [19]. Then, the setup of the MD simulations will be introduced. The modeling of

*stefan.schuett@physik.uni-greifswald.de

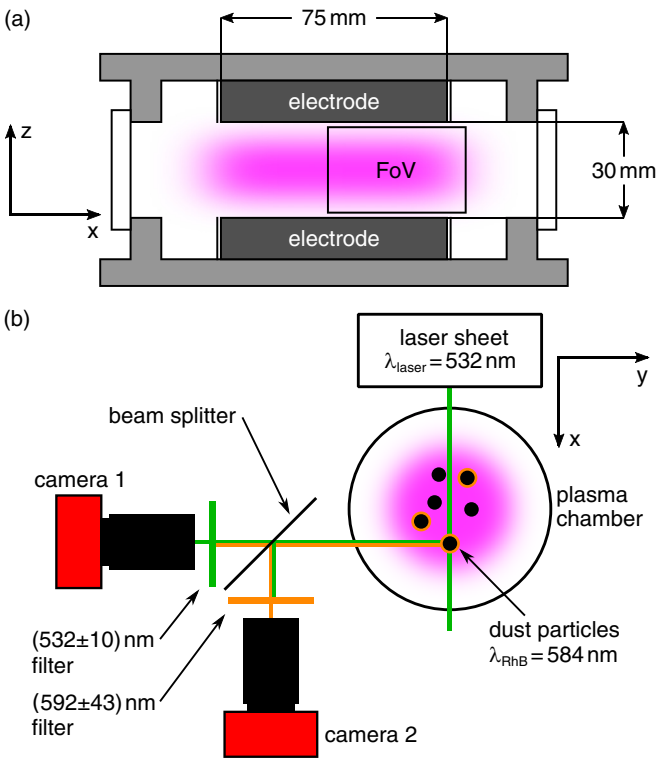

FIG. 1. Experimental setup used for the measurements under microgravity: (a) side view, (b) top view.

the experimental situation together with two adapted geometries will be presented in Secs. III, IV, and V. Finally, the simulations will be compared with the experimental results in Sec. VI.

II. SETUP OF EXPERIMENTS AND SIMULATIONS

A. Experimental setup

The experiments were performed on parabolic flights to achieve microgravity conditions and enable the formation of a three-dimensional dust cloud. Our plasma chamber is a modified version of the chamber described elsewhere [22]. The experimental setup is depicted in Fig. 1. A parallel-plate rf discharge is ignited between two electrodes with a gap of 30 mm and a diameter of 80 mm. The electrodes are driven in push-pull mode at a frequency of 13.56 MHz. The working gas is argon at pressures of 20 to 40 Pa. Dust particles are injected using electromagnetically driven shakers. Each parabola provides 22 s of microgravity, during which a single phase separation process can be measured. At the beginning of the measurement, a previously prepared mixture of two types of particles is injected. Both particle species are monodisperse melamine formaldehyde (MF) spheres. The main difference between the two species is their size. Additionally, one of the species is doped with rhodamine-B (RhB) dye.

The separation process of the two particle populations is then followed using a two-camera video microscopy setup [18,19]. The particles are illuminated by a vertically expanded laser sheet at a wavelength of 532 nm. When illuminated by the laser, the RhB particles emit fluorescence light at a wavelength of 590 nm. Two cameras observe the same field of view through a beam splitter. One of the cameras (camera 1) is equipped with a bandpass filter tuned to the laser wavelength, recording the scattered light of all particles. The other camera (camera 2) is equipped with a filter that transmits only the fluorescence light of the RhB particles. This allows to distinguish between the species even at the smallest size disparities. Particles are detected in the recorded images and their positions are determined using a moment method [23,24].

We have found from earlier experiments that the plasma conditions do not significantly influence the demixing process. Therefore, the most important variable is the size of the particles. The number of different mixtures that can be measured is limited by the number of dust shakers that can be mounted to the chamber as they cannot be exchanged during the flights. Our previous experiments [19] have been extended by measurements with more different particle sizes. For the analysis of the separation process our previous technique was refined, as described below. Also the previous data have been reanalyzed by the refined technique. In total, 228 measurements obtained during the course of four parabolic flight campaigns have been used and analyzed here.

B. Simulation and assessment of plasma forces

The main plasma-mediated forces on the particles generally are the ion drag force and the electric field force. To model those forces, a simulation of the underlying ion and electron properties in the plasma has been performed using the SIGLO code (SIGLO-2D version 1.1, Kinema Software 1996–2003) [25]. The simulations have been performed for parameters which correspond to typical parameters of our experiment. The geometry of the plasma vessel was modelled as closely as possible. We used the gas parameter data for Argon shipped with SIGLO and a neutral gas temperature of 300 K. Unless otherwise noted, the neutral gas pressure was $p = 30$ Pa and the rf peak-to-peak voltage was $U_{\mathrm{rf}} = 75$ V at a frequency of 13.56 MHz.

The simulation yields the spatially resolved plasma potential V, the electron temperature T_e and the electron and ion densities, n_e and n_i, respectively. The ion temperature is assumed as $T_i = 300$ K. Figures 2(a) and 2(b) show the electron density and temperature as obtained from the SIGLO simulation. SIGLO tends to produce slightly vertically asymmetric results. Therefore, an average of the top and bottom half is used for further calculations.

For our conditions (Argon, $T_e \approx 100\,T_i$, $p = 30$ Pa), ion-neutral collisions have to be taken into account. The floating potential that a spherical dust particle attains in the presence of collisions [26–28] is approximately $\phi_{\mathrm{fl}} = -\hat{\phi} k_B T_e / e$ with $\hat{\phi} = 1$. Here k_B is the Boltzmann constant and e is the elementary charge. Collisionless OML theory would yield $\hat{\phi} = 2.4$. Applying a capacitor model for the dust, the resulting dust charge number is

$$Z_d = 4\pi\varepsilon_0 a \phi_{\mathrm{fl}} / e, \tag{1}$$

where ε_0 is the vacuum permittivity and a is the particle radius. With this, a particle with $a = 3.5$ μm attains a charge of $Z_d = 9460$ at the center of our simulated discharge, which is realistic [26–29].

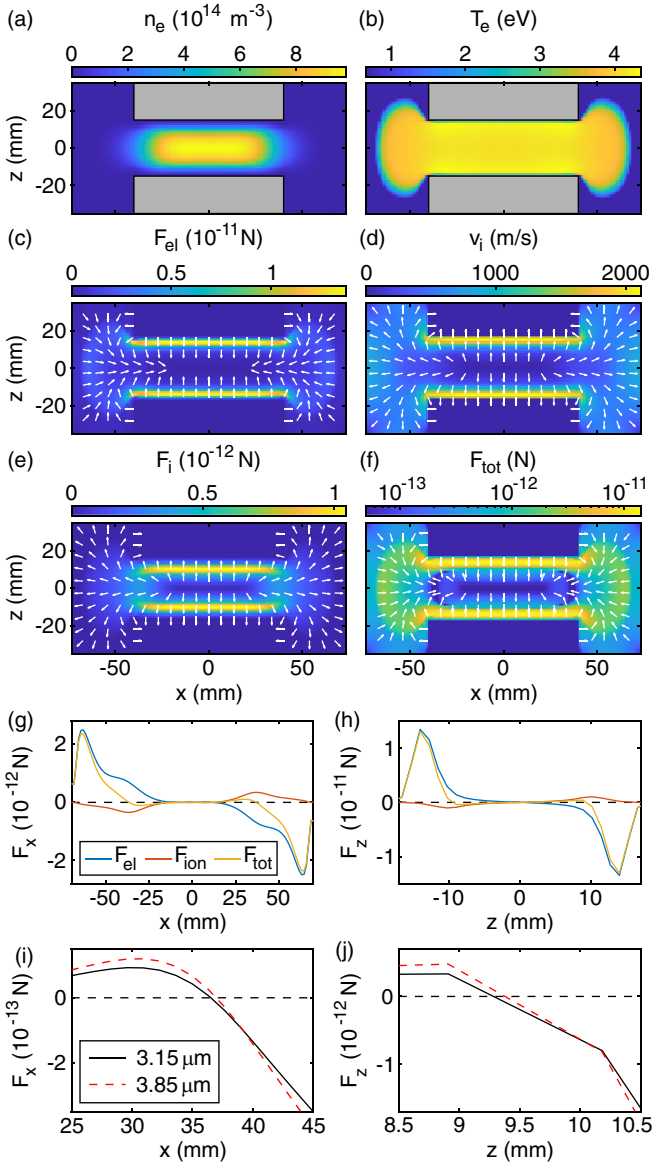

FIG. 2. Different quantities that are either provided directly by the SIGLO code or deduced from those quantities; see text for details. The gray boxes depict the location of the two electrodes. Shown are (a) the electron density, (b) the electron temperature, (c) the electric field force, (d) the ion streaming velocity, (e) the ion drag force on particles with $a = 3.5$ μm, and (f) the total force on those particles. The arrows indicate the direction of the ion streaming velocity and the forces. Their length is normalized. Panels (g) and (h) show the ion drag force along the horizontal x and vertical z axis; note the different scales. Panels (i) and (j) represent zoomed-in views of the total force on particles with $\bar{a} = 3.5$ μm and $\varepsilon = 0.2$.

The electric field force $F_{\rm el}$ on the dust is calculated directly from the plasma potential V via

$$\vec{F}_{\rm el} = Z_d e \vec{\nabla} V, \tag{2}$$

where $\vec{E} = -\vec{\nabla} V$ is the electric field. The resulting electric field force on particles with $a = 3.5$ μm can be seen in Fig. 2(c).

For the assessment of the ion drag force, again, ion-neutral collisions have to be taken into account. Hutchinson and Haakonsen have found that the ion drag force increases significantly over the collisionless ion drag when ion-neutral collisions are present [30]. First, we derive the collisionless ion drag force. We follow the procedure described by Hutchinson [31] and Khrapak *et al.* [32,33], with the addition of the collection force from Barnes *et al.* [34]. First, due to the relatively high gas pressure, from the electric field the ion streaming velocity is calculated as

$$\vec{v}_i = \mu_i \vec{E} \tag{3}$$

using a modified form of Frost's ion mobility [35,36]

$$\mu_i = 1.68 \times 10^{19} \left[1 + \left(7 \times 10^{18} \frac{E}{n_n} \right)^{1.238} \right]^{-1.238/2} \frac{E}{n_n}, \tag{4}$$

where n_n is the neutral gas number density.

The ion drag force consists of the orbit force $F_{\rm coul}$ and the collection force

$$F_{\rm coll} = \pi a^2 m_i v_s n_i v_i \left(1 - \frac{2e\phi_{\rm fl}}{m_i v_s^2} \right) \tag{5}$$

with $v_s = (v_i^2 + 4v_{T,i}^2/\pi)^{1/2}$ and the ion thermal velocity $v_{T,i} = (2k_B T_i/m_i)^{1/2}$.

The shielding efficiency of the streaming ions depends on their flow velocity. The effective screening length is taken from Hutchinson [31] as

$$\lambda_{\rm eff} = \left(\frac{\lambda_{\rm De}^2}{1 + 2k_B T_e/m_i v_{\rm eff}^2} + a^2 \right)^{1/2}, \tag{6}$$

where $\lambda_{\rm De}$ is the electron Debye length, given by $\lambda_{\rm De}^2 = \varepsilon_0 k_B T_e/n_e e^2$. The effective ion velocity $v_{\rm eff}$ is given by

$$v_{\rm eff}^2 = v_{T,i}^2 + v_i^2 \left\{ 1 + \left[\frac{v_i/v_B}{0.6 + 0.05 \ln (m_i/m_p)} \right]^3 \right\}, \tag{7}$$

where $v_B = (k_B T_e/m_i)^{1/2}$ is the Bohm velocity and m_p is the proton mass. Hutchinson's approximation $T_e = 100 T_i$ is well suited in our case [see Fig. 2(b)].

With that, the collisionless orbit force can be written as [31]

$$F_{\rm coul} = 8\pi a^2 n_i G(u) \ln \Lambda \frac{e^2 \phi_{\rm fl}^2}{m_i v_{T,i}^2}. \tag{8}$$

Here, $\ln \Lambda$ is the Coulomb logarithm and $G(u)$ is the Chandrasekhar function

$$G(u) = \frac{1}{2u^2} \left[\mathrm{erf}(u) - \frac{2u}{\sqrt{\pi}} \exp(-u^2) \right] \tag{9}$$

with $u = v_i/v_{T,i}$. The Coulomb logarithm is given by [32]

$$\ln \Lambda = \ln \frac{b_{90} + \lambda_{\rm eff}}{b_{90} + a}, \tag{10}$$

where $b_{90} = Z_d e^2/4\pi\varepsilon_0 m_i v_{\rm eff}^2$ is the impact parameter for 90° scattering. The collisionless ion drag force finally becomes $F_i = F_{\rm coll} + F_{\rm coul}$.

Now we consider the increase due to collisions. Hutchinson and Haakonsen have performed extensive numerical simulations to determine the increase over the collision-free case [30]. For our situation, the ion-neutral collision frequency

is $\nu_{\text{in}} = e/m_i\mu_i = 4.8$ MHz at a typical position in the bulk plasma. From the SIGLO data, we find the electron Debye length to be about 600 μm. Under above assumption $\hat{\phi} = 1$, the cutoff radius becomes $r_c \approx 85$ μm (see Ref. [30] for an explanation of the cutoff radius). This finally leads to the collisionality $\nu_{\text{in}} r_c/c_s = 0.15$, where the ion sound speed c_s equals the Bohm velocity. For our particles, the ratio λ_{De}/a lies between 133 ($a = 4.5$ μm) and 300 ($a = 2$ μm). In our system, the ions stream against a stationary neutral gas background where the ions follow the drift distribution. For our value of the collisionality, this results in a collisional force factor (that gives the increase of the ion drag compared to the collision-free case) of 2.

We therefore use $F_{\text{tot}} = F_{\text{el}} + 2F_i$ as the total force (where F_i is the collisionless ion drag force described above). The ion streaming velocity, the (collisionless) ion drag force and the total resulting force on dust particles with $a = 3.5$ μm are shown in Figs. 2(d) to 2(f), respectively. The forces show the characteristic shapes that lead to the formation of the void. F_i has its maximum between the center of the discharge and the electrodes. In this regime, where $v_i \approx 300$ m/s, the orbit force becomes most effective as a result of a balance between the number of passing ions and duration of their interaction with the particle. The electric field force, in contrast, steadily increases with increasing distance from the discharge center. The superposition of those forces acting in opposite directions thus creates a potential well where a dust cloud can be trapped in a balance of (increased) ion drag and electric field force. The Coulomb repulsion between the particles then makes for the radial extent of the dust cloud.

Figures 2(g) and 2(h) show the total force along the horizontal/radial x as well as along the vertical z direction, respectively. In both cases, it can be seen that the total force acts so that the particles are pushed outwards up to a certain position where the force vanishes and then rises again with opposite sign, pushing the particles backwards. The zoomed-in views in Figs. 2(i) and 2(j) allow a more detailed inspection. There, two species of slightly different radii are considered ($\bar{a} = 3.5$ μm, $\varepsilon = 0.2$). In the horizontal direction, the equilibrium position $F = 0$ is about $x = \pm 37$ mm. In the vertical direction, it is about $z = \pm 9.4$ mm. It can be seen that in both directions the equilibrium position of the larger species is slightly more outside than that of the smaller species. Additionally, around the equilibrium position, the force on the larger species is larger. In our previous descriptions of the phase separation processes [19], we have suspected that these two effects drive the phase separation.

Further outside (at $|x| > 40$ mm respectively $|z| > 10.3$ mm), the inward-pointing force on the larger species is larger. This should in theory repell the larger species out of the outermost parts of the dust cloud. But this far away from the equilibrium position, the forces are so high and their gradient is so steep that the dust cloud ends with a sharp outer boundary.

It has been found in the experiment that the phase separation happens preferably along the z direction. This seems reasonable from a comparison of the magnitudes of the forces along x and z. The maximum force difference between the two species is about 3×10^{-14} N at $|x| = 30$ mm (compared to the total force 1.2×10^{-13} N) in x. In z, the difference is 1.4×10^{-13} N and the total force is 4×10^{-13} N [$\varepsilon = 0.2$; see Figs. 2(i) and 2(j)]. As expected from the geometry, the forces are larger in z direction, leading to a larger force disparity for any given particle size and charge disparity. This will be investigated further in Sec. IV.

C. Molecular dynamics simulation

These plasma forces are now used in a molecular dynamics simulation of the dust particle motion. Molecular dynamics simulations were performed using the LAMMPS code [37], which has been proven to be a useful tool for the simulation of dusty plasmas [17,38]. Most of the simulations were run on a graphics card to greatly reduce the computation time [39–44].

The simulation is of a Langevin dynamics type. The target temperature (temperature of the heat bath) was varied between 0 and 11 000 K in a couple of test runs. While the particles' kinetic temperature quickly adopts the temperature of the heat bath, no substantial influence of the temperature on the phase separation has been found; see also Appendix. The temperature was chosen to be $T = 1000$ K for the subsequent simulations.

The two species carry the (different) charges Q_1 and Q_2 due to their size difference as discussed above in Eq. (1). Then, the interaction energy is of a shielded Coulomb (Yukawa) type,

$$V(r) = \frac{Q_1 Q_2}{4\pi\varepsilon_0 r} \exp\left(-\frac{r}{\lambda_S}\right), \tag{11}$$

for a pair of different particles, spaced at a distance r. For particles of the same species, the numerator of the first term of course becomes Q_1^2 or Q_2^2. The screening length is chosen as $\lambda_S = 300$ μm, which is a typical value for the outer bulk (where the dust is located) of our simulated discharge according to Eq. (6). When calculating the interparticle forces, the potential is cut off at $3\lambda_S$.

Further, neutral gas friction of the dust motion is taken into account. For the assessment of the neutral gas drag, we use the well-established Epstein formula

$$\beta = \delta \frac{8}{\pi} \frac{p}{a\rho_d v_{\text{th},n}} \tag{12}$$

for the friction coefficient [45]. Here $v_{\text{th},n} = (8k_B T/\pi m_n)^{1/2}$ is the neutral thermal velocity with T being the neutral gas temperature and m_n the mass of an argon atom. The coefficient δ is between 1 and 1.44 depending on the type of scattering (diffuse/specular) of the neutral atoms by the dust particles. It was found that a value of $\delta = 1.44$ is appropriate for dusty plasmas [46].

For the ion drag and electric field forces, a force field that contains the spatially dependent sum of those forces on the used particle types is calculated prior to the simulation run. In each time step, this force field is interpolated onto the particle positions and applied as an additional force before the integration step. The same method is used for the particle charge. The spatially dependent charge is interpolated onto the particle positions and updated each time step. The time step is 50 μs and the positions and velocities of all particles are stored every 10 ms for further analysis.

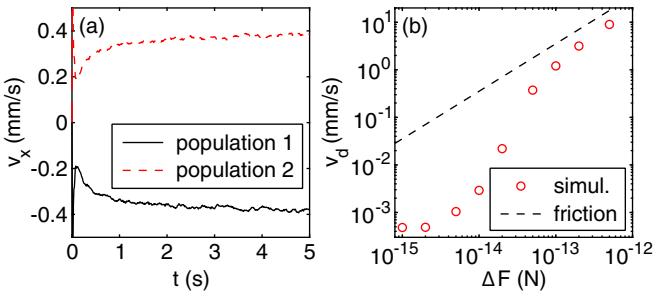

FIG. 3. (a) Drift velocity of the two species of particles, averaged over all particles in each time step. The force disparity is $\Delta F = 5 \times 10^{-14}$ N in this example. (b) Drift speed (red circles) versus force disparity ΔF. For the smallest forces, there is hardly any drift. From about $\Delta F = 10^{-14}$ N on, the drift speed starts to approach the Epstein friction limited drift speed (dashed line), but does not reach it.

III. LINEAR GEOMETRY

The resulting force field is quite complex and not curl free. To separate the various influences, we start the discussion of phase separation in simpler geometries.

An interesting question is the role of the neutral drag versus Coulomb inter-particle interaction under the action of a constant separation force during the demixing process. To assess which effect determines the final drift speed, simulations with a simple slab geometry have been performed. The simulation volume was a cuboid with a volume of $40 \times 20 \times 0.4$ mm^3. Periodic boundary conditions have been used in all dimensions. The thickness of the simulated slice (0.4 mm) was chosen as a compromise between computing time and simulating a true three-dimensional system. A total amount of 20 000 particles was simulated, 10 000 particles per species. The particles are randomly positioned at the beginning of the simulation. Then, the simulation is run for 5 s (simulated time) with the Coulomb interaction only, allowing the system to reach an equilibrium state. Afterwards, a constant separation-driving force in the x direction is switched on, starting the simulated phase separation. This way, the process can be followed from the beginning without any superimposed motion due to the stabilization of the dust cloud.

In this simulation, all particles have the same radius ($a = 3.5\ \mu$m) and fixed charge ($Z_d = 7000$). However, the two randomly distributed species experience opposite separation forces. The force on particles of species #1 is $\vec{F} = -\Delta F/2\ \hat{e}_x$ and the force on particles of species #2 is $\vec{F} = +\Delta F/2\ \hat{e}_x$, where $\hat{e}_x$ is the unit vector in x direction. Simulation runs have been performed for different values of the force disparity ΔF. For consistency with the other simulated geometries, we used $T = 1000$ K and the neutral friction coefficient $\beta = 52$ corresponding to $p = 30$ Pa.

The resulting mean drift velocities of the two populations, $v_{x,1}$ and $v_{x,2}$, respectively, are shown in Fig. 3(a). As an example, the result for $\Delta F = 5 \times 10^{-14}$ N is shown. Due to the symmetry of the external forces, the resulting velocities are symmetric around $v = 0$. The force is switched on at $t = 0$. In the initial phase of about 120 ms, the particles move to new equilibrium positions in their local confinement potential that is constituted by the neighboring particles. Afterwards, v settles to its final value of about 0.4 mm/s when the two populations each begin to move collectively against each other. This happens in the first second and after that, there is only a slight further increase of v. The Epstein time $1/\beta = 19$ ms is about one order of magnitude smaller than the timescale of the settling of v, indicating that Coulomb collisions significantly contribute to the particle dynamics.

This overall behavior is comparable between all values of ΔF. Therefore, the time average of all data points with $t > 2$ s is considered to measure the final drift speed v_d. The drift speed versus the force disparity is depicted in Fig. 3(b). While there is hardly any drift at the smallest forces, v_d rapidly increases between $\Delta F = 5 \times 10^{-15}$ N and $\Delta F = 5 \times 10^{-14}$ N. At even higher forces, v_d increases approximetely linearly with ΔF.

Next, we evaluate the drift speed that would be expected for a drift limited by neutral drag. It can be easily obtained from the balance between neutral drag force and the applied external force, i.e.,

$$\frac{\Delta F}{2} = m_d \beta v_d, \tag{13}$$

where m_d is the dust mass. This yields a drift speed of $v_d = 1.8$ mm/s for the situation shown in Fig. 3(a). Hence, the real drift speed is about a factor of 4.5 below this value. The neutral drag-limited drift speed is shown as dashed line in Fig. 3(b). The real drift speed is below the drag limit for all values of ΔF, which shows that Coulomb collisions play an important role in jamming the particle motion. At very low forces, the force is not strong enough to break the Coulomb blockade at all. Then, there is an intermediate regime where a notable particle motion onsets. At the larger forces considered here, the drift speed is about half of the value expected for a system exhibiting only Epstein drag. Similar situations where oppositely charged "plus- and minus-charge" particles are exposed to the same external field have already been studied earlier and a similar overall behavior was found [47,48]. However, interestingly, we did not find distinct lane formation in our simulations, which could further enhance particle transport.

IV. RADIAL GEOMETRY

To further assess the role of different forces in the phase separation process, we performed simulations with a synthetic, vortex-free but divergent force field. The force field is chosen cylindrically symmetric and constructed from the force profile from the SIGLO simulation along one spatial coordinate, i.e., the radial force is taken as either $F_x(x)$ or $F_z(z)$ as in Figs. 2(g) or 2(h). This allows us to investigate the asymmetry of the phase separation behavior between the x and z direction that was found in the experiment. A full set of simulation runs has been performed for both force profiles, mean particle radii of $\bar{a} = 2\ \mu$m, 3.5 μm, and 4.5 μm and size disparities between $\varepsilon = 0.01$ and $\varepsilon = 0.2$. The radii of the two species were chosen symmetrically to the mean size.

Due to the strong difference in the forces along x and z the simulated systems have a different size when using either of the force profiles. Hence, it is necessary to perform a

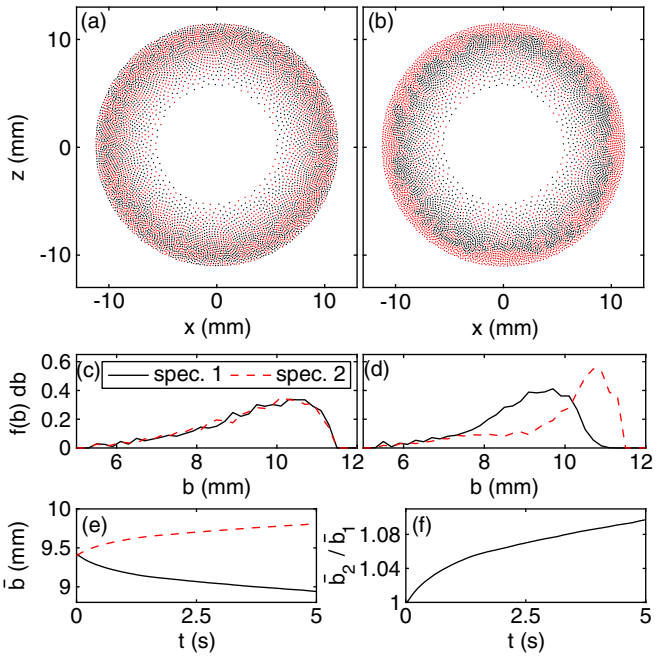

FIG. 4. Simulation with a cylindrical geometry that was constructed from the force along the z axis. The two species of particles have radii of $a_1 = 3.15\ \mu$m and $a_2 = 3.85\ \mu$m. (a) snapshot of the system after initialization. Particles of species 1 (black) and species 2 (red) are mixed. (b) Snapshot after running for 5 more seconds with force disparity. The populations are separated and a phase boundary can be seen. [(c) and (d)] Radial particle distributions for the situations shown in (a) and (b), respectively. (e) Evolution of the radial positions and (f) ratio of the radial positions of the two populations. All these quantities show an increasing separation of the two populations with time.

dedicated initialization run for each geometry. The simulation box has a volume of $120 \times 0.4 \times 120\ \text{mm}^3$, which is large enough to accommodate the system for both force profiles. The system is radially symmetric in x and z, periodic boundary conditions are used in y direction. The interparticle spacing is determined by the Coulomb interaction forces and hence depends on the (mean) particle radius via the dust charge. We performed some test runs to estimate the particle number density and assess the number of particles needed to generate dust systems of comparable size regardless of the mean particle size. To initialize the system, forces and charges for the mean particle size $\bar{a}$ are applied until an equilibrium is reached after 5 s of simulated time. Then, the charges $Z_{\text{d}1}$ and $Z_{\text{d}2}$ and respective forces for sizes a_1 and a_2 are switched on. The activation of the force disparity marks the time $t = 0$.

Figure 4 shows the results of the run with $\bar{a} = 3.5\ \mu$m and $\varepsilon = 0.2$ using the force from the z direction [Fig. 2(h)] as the radial force. The system consists of $N = 6000$ particles. An example with a relatively large size disparity was chosen that features a distinct phase separation to demonstrate the behavior of the system. Figures 4(a) and 4(b) show the system at $t = 0$ and at $t = 5$ s, respectively. Both populations are completely mixed in Fig. 4(a). In Fig. 4(b), there are two concentric shells each containing nearly exclusively particles of one of the species. The larger species accumulates in the

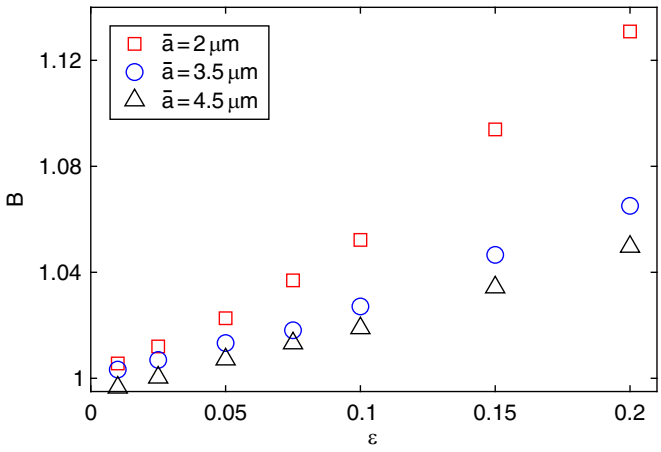

FIG. 5. Temporally averaged mean distance ratio B vs. relative size disparity ε for all simulation runs of a radial geometry with the force profile taken from the z axis (see text for details).

outer shell. Additionally, there is a central region where both species stay mixed. As the phase separation happens in radial direction, the radial position is a good quantity for further analysis. For each particle i at position (x_i, z_i), the radial position $b(i,t) = (x_i^2 + z_i^2)^{1/2}$ is calculated.

The distributions of the radial positions $f(b)db$ of the two species are a measure for the behavior of the two populations. They are shown in Figs. 4(c) and 4(d) for the time steps corresponding to the snapshots in Figs. 4(a) and 4(b). It can be seen that they reflect the situation well: At $t = 0$, the distributions are neary identical, showing the mixed state of the system. At $t = 5$ s, the distributions are split in the outer region, they are narrower and their overlap is reduced. From the center to about $b = 7.5$ mm, the overall forces are too small to drive the phase separation and the distributions match.

Next, the radial positions of all particles are averaged per population, yielding the mean radial positions of the two populations $\bar{b}_1(t)$ and $\bar{b}_2(t)$. These are good indicators for the behavior of the respective species as a whole. As can be seen in Fig. 4(e), $\bar{b}_1(t)$ and $\bar{b}_2(t)$ start at the same value at $t = 0$, indicating that both species were initialized to the same average position and are fully mixed. During the run, $\bar{b}_1(t)$ decreases whereas $\bar{b}_2(t)$ increases, meaning that the (smaller) particles of species 1 gather in the inner regions and the (larger) particles of species 2 in the outer.

The ratio $\bar{b}_2(t)/\bar{b}_1(t)$, see Fig. 4(f), enables us to use a single quantity to describe the phase separation. As time progresses, an increasing ratio indicates that the smaller population accumulates at the inside and the larger population accumulates at the outside of the system. The temporally averaged ratio $B = \langle \bar{b}_2(t)/\bar{b}_1(t) \rangle_t$ thus is a single number that characterizes a run: A faster separation as well as a more pronounced separation both lead to a larger temporally averaged mean distance ratio. We have already used this parameter B for the analysis of our previous experiments, facilitating comparisons [19].

The averaged mean distance ratios B of all runs with the radial force taken from the z profile are shown in Fig. 5 against the size disparity ε. A phase separation ($B > 1$) can be seen for $\bar{a} = 2\ \mu$m and $\bar{a} = 3.5\ \mu$m even at the smallest $\varepsilon = 0.01$

considered here. The phase separation in terms of B is more pronounced for larger ε. This trend is expected since for larger ε the force disparity increases, leading to a more pronounced separation. Furthermore, there is an influence of the absolute particle size: The larger the mean particle size at a fixed ε, the less intensive the phase separation is. From evaluating the forces as shown in Figs. 2(i) and 2(j) at different mean radii $\bar{a}$ we find that the force disparity scales about linearly with $\bar{a}$. In contrast, the Coulomb blockade as well as the neutral gas drag that obstruct the phase separation both scale with $\bar{a}^2$. Thus, the simulations with larger $\bar{a}$ show less phase separation.

When using the force profile taken from the x axis, no phase separation is found. As mentioned in Sec. II B, the force difference is about five times larger along the z axis compared to the x axis. The value of the force difference along z (1.4×10^{-13} N) lies just at the beginning of the regime where the drift speed approaches the neutral drag limit, as seen in the linear geometry. The force taken from the x axis obviously is too small to drive the separation process on the studied time scale.

V. REALISTIC GEOMETRY

Now, the full force fields from Sec. II B and Fig. 2 are used. A slice of the dust cloud is simulated, similar to the slice that is experimentally observed by the video microscopy setup. The simulation volume is a cuboid with a volume of $120 \times 0.4 \times 40$ mm^3. The particles are confined by the full force profile and the size of the simulation volume in x and z is chosen so that it can accomodate the whole dust system. In the y direction, periodic boundary conditions are used as before. It should be noted that in comparison to the experiment, where the observed slice is a section of a toroidal system, the toroidal character of the geometry was neglected here. For the initialization, as before, the force profile for particles with the mean size of the two species is calculated and applied to both species for 5 s. Afterwards, the correct force fields with the slightly different forces on the two species are applied and the simulation is run for another 5 s. Again, $t = 0$ indicates the assignment of the individual particle forces.

The results for a simulation run with particles of radii $a_1 = 3.15$ μm and $a_2 = 3.85$ μm, respectively, are depicted in Fig. 6. Trajectories are shown in Fig. 6(a). It can clearly be seen that the particle motion is dominated by vortex structures that are generated because of the nonvanishing curl of the force field [49–51]. These vortices have also been observed in our experiments and pose a problem for the analysis of the phase separation using Fick's law. The drift speeds associated with the vortices are of the order of 1 mm/s, which is greater than the typical drift speed due to the phase separation. The above described analysis using the particle distributions helps to overcome this problem [19]. To start the analysis, Figs. 6(b) and 6(c) show snapshots of a system directly after initialization ($t = 0$) and at the end of the run ($t = 5$ s). A run with the same particle sizes as in Fig. 4 is shown here.

In vertical direction, the behavior is very similar to the radial geometry: Close to the void, there is a mixed region. Further outside there is a region where preferably the smaller particles (species 1) accumulate. Finally, the larger particles (species 2) preferably accumulate at the top and bottom of the discharge. In the horizontal direction, however, there is no clear tendency towards a separated state. The asymmetric behavior between x and z direction is consistent with our findings from the previous sections, where we concluded that the force difference along the z direction is large enough to effectively drive the separation, while this is not the case along the x direction.

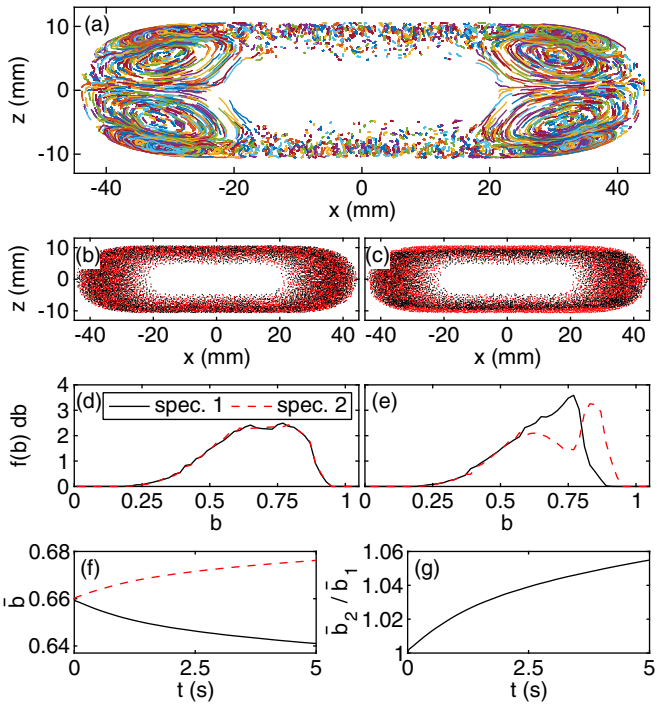

FIG. 6. Example of a simulation run for particles with $a_1 = 3.15$ μm and $a_2 = 3.85$ μm: (a) Trajectories of particles of both species from $t = 0$ to $t = 5$ s. For clarity, only every 10$^{\text{th}}$ trajectory is shown. (b) Particle positions of species 1 (black) and species 2 (red) at the beginning of the phase separation. Here every third particle is shown. (c) Same as in (b), but situation at the end of the simulation run. Particles of the larger species mainly accumulate at the top and bottom of the discharge while particles of the smaller species accumulate closer to the void. [(d) and (e)] Distribution $f(b)db$ of the radial positions of both populations at $t = 0$ and $t = 5$ s, respectively. (f) Mean radial positions $\bar{b}_{1/2}$ of the two populations and (g) their ratio $\bar{b}_2/\bar{b}_1$. At $t = 0$, a ratio of 1 and identical distributions indicate a mixed system. A progressively increasing ratio as well as a shift of the distributions in opposite direction correspond to the increasing separation of the two populations.

The analysis of the separation is performed analogously to Sec. IV and Ref. [19]. Here ellipsoidal coordinates are chosen that follow the shape of the cloud. Details can be found in Ref. [19]. The ellipsiodal position

$$b(i,t) = \frac{1}{12\ \text{mm}}\left[\left(\frac{|x_i| - \min\left(|x_i|, 12\ \text{mm}\right)}{4}\right)^2 + z_i^2\right]^{1/2} \tag{14}$$

is calculated so that it indicates whether the particle is close to the center of the discharge ($b = 0$) or further out ($b \approx 1$ for a particle at the outer edge of a typical dust cloud). The distributions [see Figs. 6(d) and 6(e)] show the transition from a mixed state with identical distributions at $t = 0$ to a separated

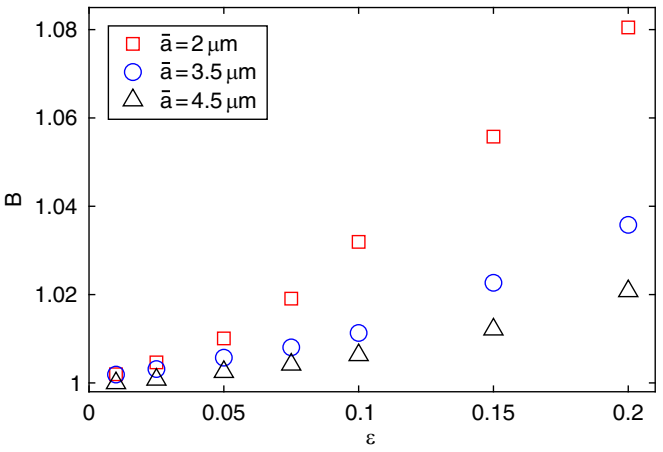

FIG. 7. Temporally averaged mean distance ratio B of all simulation runs using the realistic geometry vs relative size disparity ε.

state at $t = 5$ s, where the distributions are narrower and do not completely overlap at $b > 0.6$. Also, the mean positions of both populations [Fig. 6(f)] and their ratio [Fig. 6(g)] indicate an advancing phase separation with species 1 accumulating on the inside and species 2 on the outside. The similar shape of the distributions and $\bar{b}$ compared to Fig. 4 suggest that there are no effects that directly or indirectly depend on the geometry and influence the phase separation significantly. Especially, the curl in the force field and the resulting intense vortex motion has only a limited impact on the phase separation.

Again, we have performed simulation runs for different absolute particle sizes and size disparities. The needed amount of particles for each mean size is again estimated from some test runs. We finally used $N_0 = 40\,000$ for $\bar{a} = 2$ μm, $N_0 = 30\,000$ for $\bar{a} = 3.5$ μm, and $N_0 = 26\,000$ for $\bar{a} = 4.5$ μm. The mean distance ratios B of all runs are compiled in Fig. 7. When considering the data points belonging to the same mean radius, B increases with increasing ε, as expected. The relation is nearly linear, and a linear fit would go through the point ($\varepsilon = 0$; $B = 1$), meaning that there would be no separation if both species had the same size. The slope of this proportionality, however, depends on the absolute particle size. As above, the phase separation is stronger with larger ε or smaller absolute particle radius $\bar{a}$. Overall, the results are comparable to those with the radial geometry, supporting the hypothesis that geometric effects like the vortices do not strongly influence the phase separation.

VI. COMPARISON WITH EXPERIMENTAL DATA

In the simulations, one is able to instantly obtain the positions of the two particle species. In the experiment, however, the diagnostic setup yields the positions of only one of the species directly, namely the rhodamine-B doped species (observed via camera 2). Additionally, the positions of all particles are seen in camera 1. In the previous analysis [19], we have compared the reconstructed particle positions from "all" particles and the RhB particles and derived the separation parameters B from their data. Thus, the undoped species has not been used as an independent quantity. Here now, to

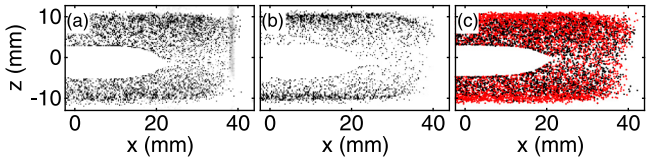

FIG. 8. Snap shots of (a) camera 1 (all particles) and (b) camera 2 (RhB particles) at a progressed state of the phase separation in data set 1. (c) Reconstructed particle positions of the RhB species seen in camera 2 (red) and the pure MF species (black). Every other particle is shown. The snap shots were inverted and their contrast enhanced.

allow for better comparison of experimental and numerical results, the positions of the undoped pure MF particles are reconstructed. This is done by measuring the positions of all particles resulting in a list of the positions of "all" particles. Now, for each RhB position, the closest "all" position is eliminated from the list if it lies within a neighborhood of 0.2 mm. The remaining particles are assumed to be the positions of the MF particles. The allowed deviation of positions of 0.2 mm accounts for an imperfect calibration of the cameras and vibrations during the flight that shift the cameras relatively to each other. Even if a particle is eliminated from the list that does not correspond to the RhB particle that caused this elimination, the maximum distance of 0.2 mm ensures that the maximum position error of the erroneously remaining "MF" particle is < 0.4 mm compared to the position of the particle that should have remained instead. Snap shots of both cameras and reconstructed particle positions are shown in Fig. 8.

It is probable that not all particles are detected. Furthermore, the fraction of detected particles may be different between the two cameras. Due to bleaching of the RhB particles, this fraction may change over time for camera 2. This would lead to incorrect number of particles assigned to the "MF" species. However, the fraction of correctly detected particles is not dependent on the position and therefore, the normalized radial distribution should not be affected by these effects.

Now, the positions of all particles, the RhB particles and the reconstructed MF particles are calculated using the ellipsoidal coordinates as in Sec. V. The mean positions of two experimental data sets is shown in Fig. 9. The corresponding

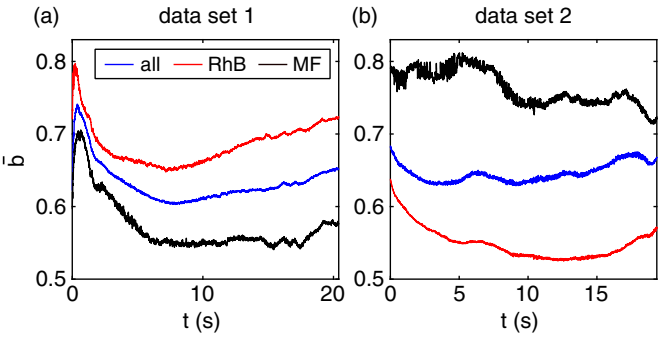

FIG. 9. Mean radial distance $\bar{b}$ of two measurements versus time. For data set 1, the RhB particles are the larger species ($\bar{d}_{\mathrm{RhB}} > \bar{d}_{\mathrm{MF}}$). For data set 2, the RhB particles are the smaller species ($\bar{d}_{\mathrm{RhB}} < \bar{d}_{\mathrm{MF}}$). In both cases, the curve for $\bar{b}_{\mathrm{all}}$ lies between $\bar{b}_{\mathrm{RhB}}$ and $\bar{b}_{\mathrm{MF}}$.

TABLE I. Particle properties of the two data sets shown in Figs. 8 and 9.

Data set	$2a_{\mathrm{MF}}$ (μm)	$2a_{\mathrm{RhB}}$ (μm)	ε
1	6.84 ± 0.07	7.12 ± 0.15	$+0.040 \pm 0.024$
2	7.01 ± 0.08	6.38 ± 0.15	-0.094 ± 0.025

particle radii and the resulting size disparities are compiled in Table I. Note that here we have defined the size disparity as the ratio of the radius of the RhB species to the radius of the unmarked species, $\varepsilon = (a_{\mathrm{RhB}} - a_{\mathrm{MF}})/\bar{a}$. Thus, $\varepsilon > 0$ indicates that the RhB particles are the larger species while $\varepsilon < 0$ indicates that the pure MF particles are the larger species. Both data sets were obtained at a pressure of 30 Pa and an rf power of 2.5 W. In addition to the positions of the RhB particles from camera 2, $\bar{b}_{\mathrm{RhB}}$, and the reconstructed MF particles, $\bar{b}_{\mathrm{MF}}$, the data from camera 1, $\bar{b}_{\mathrm{all}}$ (all particles), is shown. As opposed to the simulation, an asymmetry between the particle types might be present that is not solely caused by the size difference of the particles. Effects of the RhB dye that is present in only one of the populations as well as different particle properties due to the storage conditions are possible. Therefore, two data sets are shown here that have opposed size disparities.

In both cases, $\bar{b}$ of the smaller species is smaller than $\bar{b}$ of the larger species. $\bar{b}_{\mathrm{all}}$ lies between the other curves in both cases. The analysis has been started as early as possible after dust injection, i.e., when the dust cloud has stabilized enough to have its final shape that allows to reliably determine radial positions. At that time, the phase separation has already progressed. Hence, there is a difference between $\bar{b}_{\mathrm{RhB}}$ and $\bar{b}_{\mathrm{MF}}$ already at the beginning of the analyzed sequence. In the case of data set 1, this difference increases further. In the case of data set 2, the difference remains nearly constant. The absolute value of the relative size disparity $|\varepsilon|$ is larger for data set 2, which probably leads to a faster phase separation. Thus, the phase separation has already reached its final, separated state when the dust cloud has stabilized and the analyzed sequence starts. In contrast, the phase separation takes longer for data set 1, so that the separation process and not just its final state is reflected in the depicted curves. Furthermore, in the first 2 s of data set 1, all the $\bar{b}$ curves rapidly increase and then decrease again. This probably is a an artifact of the stabilization of the dust cloud. It is included in some data sets due to the manual selection of the start of the analyzed sequence. However, the ratio $\bar{b}_{\mathrm{RhB}}/\bar{b}_{\mathrm{MF}}$ that will be analyzed in the following is not affected by this common behavior of both populations.

Finally, the temporally averaged mean distance ratio $B = \langle \bar{b}_{\mathrm{RhB}}(t)/\bar{b}_{\mathrm{MF}}(t) \rangle_t$ of all analyzed measurements is shown in Fig. 10. We complemented our previous 175 data points from Ref. [19] with 53 new measurements from 2019 and 2020 parabolic flight campaigns. 19 of the new data points use a new mean radius of $\bar{a} = 4.5$ μm. All new points integrate nicely with the reanalyzed older data. It can clearly be seen that there is a correlation between the size disparity and the distance ratio. For $\varepsilon < 0.05$ there is a linear relationship between ε and B. One would expect $B = 1$ at $\varepsilon = 0$ because

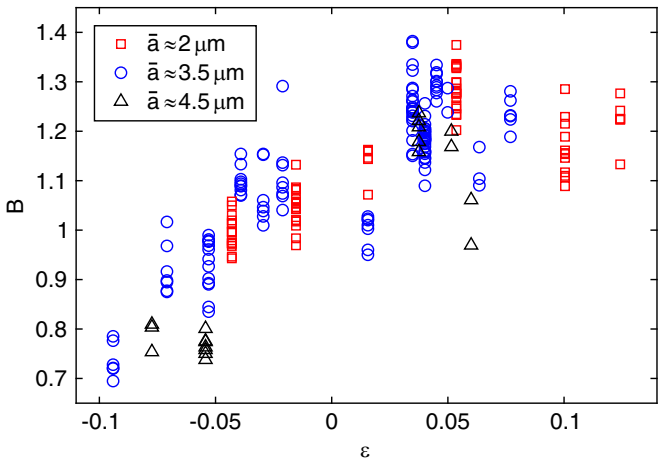

FIG. 10. Temporally averaged mean distance ratio B of all measurements vs. relative size disparity ε.

perfectly identical particles do not separate and thus yield $B = 1$. However, the curve seems slightly shifted towards higher B. Possible reasons were already discussed in Ref. [19]. Additionally, B seems to saturate at $\varepsilon > 0.05$ (but not at $\varepsilon < -0.05$), but there are not enough data points in this regime for this to be significant. In addition, the size disparity cannot be controlled in the experiment as exactly as in the simulations due to the size distribution of the manufactured particles (see Table I).

The amount of particles injected into the plasma cannot be controlled perfectly. As a result, consecutive measurements at the same parameters may use different amounts of particles and therefore produce a slightly different B. This and the inevitable residual gravity on the parabolic flight are suspected to be the main reasons for the scatter of data points at the same ε and $\bar{a}$ in Fig. 10. We performed measurements at different gas pressures and rf powers and found no significant trends [19]. This stays true with the addition of the new data. Main reason might be that the expected changes of the separation behavior with these parameters is relatively small (see Appendix). The resulting change in B then completely vanishes in the larger variations due to particle number changes and residual gravity.

These results agree with our simulations from the previous section insofar that they showed a linear relationship between ε and B, as well. Furthermore, in the simulations the phase separation in terms of B was weaker with increasing mean particle radius $\bar{a}$. Although we conducted measurements with different mean radii, we did not see this effect in the experiment. When comparing Figs. 7 and 10, it can be seen that the absolute values of B are larger in the experiment than in the simulation, i.e., the phase separation is stronger in the experiment. This suggests that the forces may be larger in the experiment. The SIGLO simulations for the force field were done for a dust-free discharge. The presence of the dust will collect electrons from the plasma and hence result in larger gradients of the plasma properties. This could lead to larger forces and force differences between the species.

At larger size disparities, it is known that binary complex plasmas feature lane formation [11–14,17]. The effect has also

been found at small size disparities when the second dust species was injected into an already existing dust cloud of the first species [18]. However, we have not observed lane formation in the experiments or simulations presented here, which is probably due to the strong vortex motion in conjunction with the slow separation dynamics.

As can be seen in Figs. 2(g) and 2(h) the ion drag force outbalances the electric field force only by a small amount in the central region. Therefore, the balance of the plasma forces versus Coulomb repulsion can change by subtle variations of parameters. We have noticed that there are parameters where some particles can enter the void. In contrast, it is known that a stable void is formed in experiments regardless of chamber geometry or exact choice of plasma conditions. This supports the hypothesis that the ion drag force may be underestimated by our method. A higher ion drag force would lead to stronger phase separation, which would be consistent with our experimental data. A more advanced (self-consistent) simulation of the dusty plasma or a more accurate calculation of the forces could improve the agreement between simulations and experiments.

VII. SUMMARY

We have investigated phase separation in binary dusty plasmas at small size disparities ($\varepsilon < 0.2$) by means of simulations. The plasma conditions were obtained from the SIGLO software and used to compute the force fields acting on the dust particles. The shape of the force profiles and their dependence on the particle size leads to a force disparity between the two particle species of slightly different size. The force disparity generally explains the radial separation of the species and the structure of the resulting dust cloud that is observed in experiments under microgravity conditions.

We have then performed Langevin dynamics simulations of binary dust systems using the LAMMPS software. First, a linear geometry with forces acting in opposite directions on the two species show that strong-coupling effects of the particles play an important role, i.e., dust-dust collisions significantly reduce the final drift speed of the particles.

The simulation of the full geometry of the microgravity experiment reproduces many of the experimental results, including the formation of vortex flows. Despite the vortex flows, we could identify phase separation even at a very small size disparity ($\varepsilon = 0.01$). The phase separation was quantified using an ellipsoidal coordinate. We have found that the phase separation is more pronounced with increasing force disparity due to increasing size disparity. At fixed size disparity, the phase separation becomes less pronounced with increasing mean particle size as a result of the interplay of forces.

By comparison with a radially symmetric, vortex-free geometry we have found that the vortices do not have a major influence on the phase separation. There is a generally good agreemment between experiment and simulation regarding a linear dependency of the separation parameter B on the size disparity ε. However, the simulation yields a dependence of the phase separation on the absolute size of the used particles, which has not been observed experimentally.

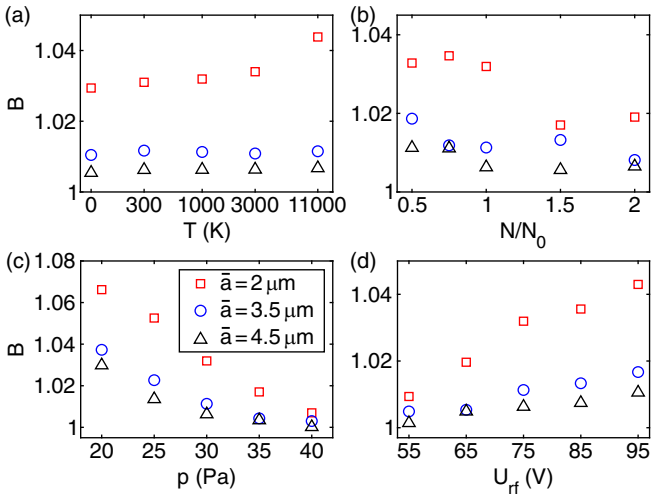

FIG. 11. Mean distance ratio B versus different parameters: (a) temperature, (b) particle number, (c) neutral gas pressure, and (d) rf voltage.

ACKNOWLEDGMENTS

Financial support by Deutsches Zentrum für Luft- und Raumfahrt under Contracts No. 50WM1638 and No. 50WM1962 is gratefully acknowledged. The authors thank Peter Druckrey for technical support. We are grateful for the comments of the referee which led to several improvements of this manuscript.

APPENDIX: RESULTS OF PARAMETER VARIATIONS

We have varied several parameters in the simulation of the realistic geometry that may directly or indirectly influence the phase separation: dust particle kinetic temperature T and particle number N in LAMMPS, neutral gas pressure p, and rf peak-to-peak driving voltage U_{rf} in SIGLO (resulting in different force fields). The default values were $T = 1000$ K, $p = 30$ Pa, and $U_{\mathrm{rf}} = 75$ V. The default particle number N_0 depends on the mean particle size and the values are given in Sec. V. The results of the simulation in terms of the separation parameter B are shown in Fig. 11. For all runs, we chose $\varepsilon = 0.1$.

In all cases, there are the expected trends: With higher temperature, the phase separation is slightly stronger, because with increasing particle motion it becomes easier for particles to penetrate the system. With increasing particle number, the particle density increases, particles exhibit more Coulomb collisions and thus the phase separation is inhibited. With increasing neutral gas pressure, the increasing neutral drag has the same effect. With higher plasma power, the ion density as well as the electric field increase, leading to increased driving forces for the phase separation.

[1] D. Beysens, P. Guenoun, and F. Perrot, Phys. Rev. A **38**, 4173 (1988).

[2] J. S. Huang, W. I. Goldburg, and A. W. Bjerkaas, Phys. Rev. Lett. **32**, 921 (1974).

[3] M. Carpineti and M. Giglio, Phys. Rev. Lett. **68**, 3327 (1992).

[4] A. E. Bailey, W. C. K. Poon, R. J. Christianson, A. B. Schofield, U. Gasser, V. Prasad, S. Manley, P. N. Segre, L. Cipelletti, W. V. Meyer, M. P. Doherty, S. Sankaran, A. L. Jankovsky, W. L. Shiley, J. P. Bowen, J. C. Eggers, C. Kurta, T. Lorik, P. N. Pusey, and D. A. Weitz, Phys. Rev. Lett. **99**, 205701 (2007).

[5] K. Yoshizawa, N. Wakabayashi, M. Yonese, J. Yamanaka, and C. P. Royall, Soft Matter **8**, 11732 (2012).

[6] S. Katano and M. Iizumi, Phys. Rev. Lett. **52**, 835 (1984).

[7] B. D. Gaulin, S. Spooner, and Y. Morii, Phys. Rev. Lett. **59**, 668 (1987).

[8] P. Wiltzius, F. S. Bates, and W. R. Heffner, Phys. Rev. Lett. **60**, 1538 (1988).

[9] M. Mikikian, L. Boufendi, A. Bouchoule, H. M. Thomas, G. E. Morfill, A. P. Nefedov, V. E. Fortov, and the PKE-Nefedov team, New J. Phys. **5**, 19 (2003).

[10] G. E. Morfill, U. Konopka, M. Kretschmer, M. Rubin-Zuzic, H. M. Thomas, S. K. Zhdanov, and V. Tsytovich, New J. Phys. **8**, 7 (2006).

[11] K. R. Sütterlin, A. Wysocki, A. V. Ivlev, C. Räth, H. M. Thomas, M. Rubin-Zuzic, W. J. Goedheer, V. E. Fortov, A. M. Lipaev, V. I. Molotkov, O. F. Petrov, G. E. Morfill, and H. Löwen, Phys. Rev. Lett. **102**, 085003 (2009).

[12] K. R. Sütterlin, H. M. Thomas, A. V. Ivlev, G. E. Morfill, A. M. Fortov, V. E. Lipaev, V. I. Molotkov, O. F. Petrov, A. Wysocki, and H. Löwen, IEEE Trans. Plasma Sci. **38**, 861 (2010).

[13] K. Jiang, C.-R. Du, K. R. Sütterlin, A. V. Ivlev, and G. E. Morfill, Europhys. Lett. **92**, 65002 (2010).

[14] C.-R. Du, K. R. Sütterlin, K. Jiang, C. Räth, A. V. Ivlev, S. Khrapak, M. Schwabe, H. M. Thomas, V. E. Fortov, A. M. Lipaev, V. I. Molotkov, O. F. Petrov, Y. Malentschenko, F. Yurtschichin, Y. Lonchakov, and G. E. Morfill, New J. Phys. **14**, 073058 (2012).

[15] M. R. Akdim, W. J. Goedheer, and R. P. Dahiya, New J. Phys. **5**, 20 (2003).

[16] A. Wysocki, C. Räth, A. V. Ivlev, K. R. Sütterlin, H. M. Thomas, S. Khrapak, S. Zhdanov, V. E. Fortov, A. M. Lipaev, V. I. Molotkov, O. F. Petrov, H. Löwen, and G. E. Morfill, Phys. Rev. Lett. **105**, 045001 (2010).

[17] M. Schwabe and D. B. Graves, Phys. Rev. E **88**, 023101 (2013).

[18] C. Killer, T. Bockwoldt, S. Schütt, M. Himpel, A. Melzer, and A. Piel, Phys. Rev. Lett. **116**, 115002 (2016).

[19] S. Schütt, M. Himpel, and A. Melzer, Phys. Rev. E **101**, 043213 (2020).

[20] J. W. Cahn, J. Chem. Phys. **42**, 93 (1965).

[21] A. V. Ivlev, S. K. Zhdanov, H. M. Thomas, and G. E. Morfill, Europhys. Lett. **85**, 45001 (2009).

[22] M. Klindworth, O. Arp, and A. Piel, J. Phys. D **39**, 1095 (2006).

[23] J. C. Crocker and D. G. Grier, J. Colloid Interface Sci. **179**, 298 (1996).

[24] Y. Ivanov and A. Melzer, Rev. Sci. Instrum. **78**, 033506 (2007).

[25] J. P. Boeuf and L. C. Pitchford, Phys. Rev. E **51**, 1376 (1995).

[26] S. Ratynskaia, S. Khrapak, A. Zobnin, M. H. Thoma, M. Kretschmer, A. Usachev, V. Yaroshenko, R. A. Quinn, G. E. Morfill, O. Petrov, and V. Fortov, Phys. Rev. Lett. **93**, 085001 (2004).

[27] S. A. Khrapak, S. V. Ratynskaia, A. V. Zobnin, A. D. Usachev, V. V. Yaroshenko, M. H. Thoma, M. Kretschmer, H. Höfner, G. E. Morfill, O. F. Petrov, and V. E. Fortov, Phys. Rev. E **72**, 016406 (2005).

[28] S. Khrapak and G. Morfill, Contrib. Plasma Phys. **49**, 148 (2009).

[29] B. Liu, J. Goree, V. E. Fortov, A. M. Lipaev, V. I. Molotkov, O. F. Petrov, G. E. Morfill, H. M. Thomas, and A. V. Ivlev, Phys. Plasmas **17**, 053701 (2010).

[30] I. H. Hutchinson and C. B. Haakonsen, Phys. Plasmas **20**, 083701 (2013).

[31] I. H. Hutchinson, Plasma Phys. Controlled Fus. **48**, 185 (2006).

[32] S. A. Khrapak, A. V. Ivlev, G. E. Morfill, and H. M. Thomas, Phys. Rev. E **66**, 046414 (2002).

[33] S. A. Khrapak, A. V. Ivlev, S. K. Zhdanov, and G. E. Morfill, Phys. Plasmas **12**, 042308 (2005).

[34] M. S. Barnes, J. H. Keller, J. C. Forster, J. A. O'Neill, and D. K. Coultas, Phys. Rev. Lett. **68**, 313 (1992).

[35] L. S. Frost, Phys. Rev. **105**, 354 (1957).

[36] S. A. Khrapak and A. G. Khrapak, AIP Adv. **9**, 095008 (2019).

[37] S. Plimpton, J. Comp. Phys. **117**, 1 (1995).

[38] M. Schwabe, S. A. Khrapak, S. K. Zhdanov, M. Y. Pustylnik, C. Räth, M. Fink, M. Kretschmer, A. M. Lipaev, V. I. Molotkov, A. S. Schmitz, M. H. Thoma, A. D. Usachev, A. V. Zobnin, G. I. Padalka, V. E. Fortov, O. F. Petrov, and H. M. Thomas, New J. Phys. **22**, 083079 (2020).

[39] W. M. Brown, P. Wang, S. J. Plimpton, and A. N. Tharrington, Comp. Phys. Comm. **182**, 898 (2011).

[40] W. M. Brown, A. Kohlmeyer, S. J. Plimpton, and A. N. Tharrington, Comp. Phys. Comm. **183**, 449 (2012).

[41] W. M. Brown and Y. Masako, Comp. Phys. Comm. **184**, 2785 (2013).

[42] T. D. Nguyen and S. J. Plimpton, Comput. Mater. Sci. **100**, 173 (2015).

[43] T. D. Nguyen, Comp. Phys. Comm. **212**, 113 (2017).

[44] V. Nikolskiy and V. Stegailov, in *Proceedings of the International Conference on Parallel Computing*, Advances in Parallel Computing, Vol. 36 (IOS Press, Amsterdam, The Netherlands, 2019), pp. 565–573.

[45] P. S. Epstein, Phys. Rev. **23**, 710 (1924).

[46] J. Carstensen, F. Haase, H. Jung, B. Tadsen, S. Groth, F. Greiner, and A. Piel, IEEE Trans. Plasma Sci. **41**, 764 (2013).

[47] M. Aertsens and J. Naudts, J. Stat. Phys. **62**, 609 (1991).

[48] J. Dzubiella, G. P. Hoffmann, and H. Löwen, Phys. Rev. E **65**, 021402 (2002).

[49] M. R. Akdim and W. J. Goedheer, Phys. Rev. E **67**, 056405 (2003).

[50] M. Schwabe, S. Zhdanov, C. Räth, D. B. Graves, H. M. Thomas, and G. E. Morfill, Phys. Rev. Lett. **112**, 115002 (2014).

[51] T. Bockwoldt, O. Arp, K. O. Menzel, and A. Piel, Phys. Plasmas **21**, 103703 (2014).